An application of the Peano series expansion to predict sound propagation in materials with continuous pore stratification

A. Geslain, J. P. Groby, and O. Dazel
Laboratoire d'Acoustique de l'Université du Maine, UMR6613 Centre National de la Recherche Scientifique/Université du Maine, F-72085 Le Mans Cedex 9, France

S. Mahasaranon, K. V. Horoshenkov,[a] and A. Khan
School of Engineering, University of Bradford, Bradford, West Yorkshire, BD7 1DP, United Kingdom

(Received 3 December 2011; revised 17 May 2012; accepted 22 May 2012)

This work reports on an application of the state vector (Stroh) formalism and Peano series expansion to solve the problem of sound propagation in a material with continuous pore stratification. An alternative Biot formulation is used to link the equivalent velocity in the oscillatory flow in the material pores with the acoustic pressure gradient. In this formulation, the complex dynamic density and bulk modulus are predicted using the equivalent fluid flow model developed by Horoshenkov and Swift [J. Acoust. Soc. Am. **110**(5), 2371–2378 (2001)] under the rigid frame approximation. This model is validated against experimental data obtained for a 140 mm thick material specimen with continuous pore size stratification and relatively constant porosity. This material has been produced from polyurethane binder solution placed in a container with a vented top and sealed bottom to achieve a gradient in the reaction time which caused a pore size stratification to develop as a function of depth [Mahasaranon *et al.*, J. Appl. Phys. **111**, 084901 (2012)]. It is shown that the acoustical properties of this class of materials can be accurately predicted with the adopted theoretical model. © *2012 Acoustical Society of America*. [http://dx.doi.org/10.1121/1.4728188]

PACS number(s): 43.50.Gf, 43.20.Bi, 43.20.El, 43.20.Hq [FCS] Pages: 208–215

I. INTRODUCTION

Porous materials are commonly used to absorb acoustic noise. These materials are typically efficient only when the acoustic wavelength (λ) is smaller or comparable to the layer thickness (L) and when there is a good match between the impedance of the surrounding fluid ($\rho_0 c$) and the surface impedance of the porous layer (z_s). As a result, the maximum absorption of a highly porous layer is typically achieved when the input resistance [$\mathrm{Re}(z_s)$] of the acoustic layer is approximately equal to the input reactance [$\mathrm{Im}(z_s)$]. In this case, the optimal flow resistivity of the layer material (R_b) is determined by the following conflicting criteria: (i) $R_b \approx 0.34\rho_0 c/(\Omega L/\lambda)$ and (ii) $R_b kL \ll 1$, where k is the wavenumber in air and Ω is the material porosity.[1] An obvious problem here is that the required thickness of the porous layer needs to increase proportionally with the increased wavelength to ensure that the latter condition remains satisfied. Since it is impractical to install acoustic absorbers which thickness is comparable with the acoustic wavelength, a majority of conventional porous absorbers are typically designed to perform well in the medium and high frequency regimes, i.e., at frequencies of 500 Hz and above.

In order to improve the low-frequency performance of a porous absorber, it is common to stack a discrete number of homogeneous porous layers to reduce gradually the mismatch between the acoustic impedance of air and the input impedance of the resultant material structure.[2] Although this technology is well established, there have been few studies which can demonstrate that an improvement in the absorption coefficient can be obtained by producing a material with continuous pore stratification, and that the acoustical properties of this structure can be accurately modeled on the basis of a limited number of measured microstructural parameters. Therefore, the purpose of this work is to fill this gap by presenting new experimental data on the acoustical and nonacoustical properties of a porous material in which continuous pore stratification has been achieved. This material is produced using a relatively simple chemical reaction process which is described in detail by Mahasaranon *et al.*[3] The obtained experimental data are then used to validate the model for the acoustical properties of porous media with pore stratification proposed recently by De Ryck *et al.*[4] The model is based on the alternative Biot's formulation[5] in which the dynamic complex density and compressibility are given by the expression in the work proposed by Horoshenkov and Swift.[6] In this way the variation in the pore size distribution data obtained for several piecewise quasi-homogeneous sub-layers can be accounted for and used to predict the acoustic behavior of the entire material specimen.

In this work the equations of macroscopically inhomogeneous porous material under rigid frame approximation are solved by use of the state vector (Stroh) formalism together with Peano series expansion described by Gautier *et al.*[7] for the full set of poroelastic equations. This may be considered as a standard method of modeling wave propagation in an anisotropic material, e.g., elastic materials with stratification[8,9] and in functionally graded materials.[10] The approach can also account for continuously varying properties in rigid frame

[a]Author to whom correspondence should be addressed. Electronic mail: k.horoshenkov@bradford.ac.uk

 0001-4966/2012/132(1)/208/8/$30.00

porous media, e.g., media with continuous pore stratification which has been recently developed by Masaharanon *et al.*[3] In this paper, the Stroh formalism/Peano series expansion method is applied for the first time to a real porous material under rigid frame approximation with pronounced continuous pore stratification. Henceforth, problems related to a coarse parameter discretization, which are common in the case of a standard transfer matrix approach (e.g., the model used by Mahasaranon *et al.*[3]) can be avoided.

II. EQUATIONS OF MACROSCOPICALLY INHOMOGENEOUS POROUS MATERIALS UNDER THE RIGID FRAME APPROXIMATION

Rather than dealing directly with the temporal representation of the acoustic field in a porous inhomogeneous layer, $\bar{s}(\mathbf{x},t)$ [with $\mathbf{x}=(x_1,x_2)$], we will prefer to deal with its Fourier transform, $s(\mathbf{x},\omega)$. These representations are related by $\bar{s}(\mathbf{x},t)=\int_{-\infty}^{\infty}s(\mathbf{x},\omega)e^{i\omega t}d\omega$, wherein $\omega=2\pi\nu$ is the angular frequency, with ν being the frequency. Henceforth, we drop the ω in $s(\mathbf{x},\omega)$ and will refer further in this paper to the Fourier transform of $\bar{s}(\mathbf{x},t)$ as $s(\mathbf{x})$.

De Ryck *et al.* used the alternative Biot's formulation[5] to derive the equations of motion in a macroscopically inhomogeneous porous material under the rigid frame approximation.[4] Under the rigid frame approximation we assume the regime whereby the material frame is sufficiently rigid and dense to be immobile in response to an incident sound pressure wave. In this case, the governing equations take the following form:

$$\begin{cases} i\omega p=\tilde{K}_{eq}(\mathbf{x})\nabla\cdot\mathbf{V}, \\ i\omega\tilde{\rho}_{eq}(\mathbf{x})\mathbf{V}=\nabla p, \end{cases} \tag{1}$$

where p is the fluid pressure in the material pores and $\mathbf{V}$ is the equivalent velocity vector for the oscillatory fluid flow in the interconnected pores. This equivalent velocity vector is related to the velocity vector of the fluid $\mathbf{V}^f$ through $\mathbf{V}=\Omega\mathbf{V}^f$, where Ω is the open porosity defined as a ratio of the volume of open, interconnected pores to the total volume occupied by the material sample. Here, the porous medium can be assumed to behave as an equivalent fluid with the equivalent, frequency and space dependent fluid density, $\tilde{\rho}_{eq}$, and bulk modulus, $\tilde{K}_{eq}$. These quantities account for the viscous and thermal losses in the pores which size varies with depth. Rather than using the common Johnson–Champoux–Allard model,[11,12] the model of Horoshenkov and Swift[6] is adopted which assumes a close to log-normal distribution of pore size. This model can account well for a relatively broad pore size distribution which is typically found in polyurethane foams which comprise a relatively large proportion of recycled fibers and grains.[13] According to this model, the equivalent density and compressibility are defined by

$$\tilde{\rho}_{eq}(\mathbf{x},\omega)=\frac{q(\mathbf{x})^2}{\Omega(\mathbf{x})}\left(\rho_f-\frac{\Omega(\mathbf{x})R_b(\mathbf{x})}{i\omega q(\mathbf{x})^2}\tilde{F}(\mathbf{x},\omega)\right),$$

$$1/\tilde{K}_{eq}(\mathbf{x},\omega)=\frac{\Omega(\mathbf{x})}{\gamma P_0}\left(\gamma-\frac{\rho_f q(\mathbf{x})^2(\gamma-1)}{\Omega(\mathbf{x})\tilde{\rho}_{eq}(\mathbf{x},\mathrm{Pr}\omega)}\right), \tag{2}$$

where γ is the specific heat ratio, P_0 is the atmospheric pressure, ρ_f is the density of the saturating fluid, Pr is the Prandtl number, q^2 is the tortuosity, and R_b is the static flow resistivity. In the case of a material with a log-normal pore size distribution, the viscosity correction function $F(\omega)$ can be approximated as

$$\tilde{F}(\mathbf{x})\approx\frac{1+a_1(\mathbf{x})\tilde{\varepsilon}(\mathbf{x})+a_2(\mathbf{x})\tilde{\varepsilon}(\mathbf{x})^2}{1+b_1(\mathbf{x})\tilde{\varepsilon}(\mathbf{x})}, \tag{3}$$

where $\tilde{\varepsilon}(\mathbf{x})=(-i\omega\rho_f q(\mathbf{x})^2/R_b(\mathbf{x})\Omega(\mathbf{x}))^{1/2}$, $a_1(\mathbf{x})=\theta_1(\mathbf{x})/\theta_2(\mathbf{x})$, $a_2(\mathbf{x})=\theta_1(\mathbf{x})$, and $b_1(\mathbf{x})=a_1(\mathbf{x})$. The pores are assumed to be cylindrical so that the coefficients $\theta_1(\mathbf{x})=4e^{4\zeta(\mathbf{x})}/3-1$, $\theta_2(\mathbf{x})=e^{3\zeta(\mathbf{x})/2}/\sqrt{2}$ in approximation (3), are controlled by the depth-dependent value of the standard deviation in the log-normally distributed pore size, $\sigma(\mathbf{x})$, i.e., $\zeta(\mathbf{x})=(\sigma(\mathbf{x})\log 2)^2$.

III. NUMERICAL EVALUATION OF THE PRESSURE FIELD

A. Description of the configuration

Both the incident plane acoustic wave and the plate are assumed to be invariant with respect to the Cartesian coordinate x_3. A cross-sectional $(x_1;x_2)$ plane view of the 2D scattering problem is shown in Fig. 1.

The upper and lower boundaries of the layer are flat and parallel. They are designated by Γ_L and Γ_0 and their x_2 coordinates are L and 0, respectively. Porous material $M^{[1]}$ occupies the domain $D^{[1]}$. The inhomogeneity (stratification) of the material layer occurs along the x_2 direction, i.e., Ω, q^2, R_b, and σ are x_2 depth-dependent as suggested in Eq. (2). The material can be viewed either as a functionally graded material or as a multilayer when the properties are piecewise constant. The surrounding and saturating fluid is air (density $\rho_f=1.213\,\mathrm{kg\,m^{-3}}$, Prandtl number $\mathrm{Pr}=0.71$, and atmospheric pressure $P_0=1.013\,25\times10^5$ Pa). The inhomogeneous porous layer is backed by a rigid plate at Γ_0.

We denote the total pressure, wavenumber, and wave speed by the generic symbols p, k, and c, respectively, with $p=p^{[j]}$, $k=k^{[j]}=\omega/c^{[j]}$ in $D^{[j]}$, $j=0,1$. The wavevector $\mathbf{k^i}$ of the incident plane wave lies in the sagittal plane and the angle of incidence is θ^i measured counterclockwise from the positive x_1 axis. The incident wave initially propagating in $D^{[0]}$ is expressed by $p^i(\mathbf{x})=e^{i\left(k_1x_1-k_2^{[0]}(x_2-L)\right)}$, wherein $k_1=-k^{[0]}\cos\theta^i$ and $k_2^{[0]}=k^{[0]}\sin\theta^i$. The uniqueness of the

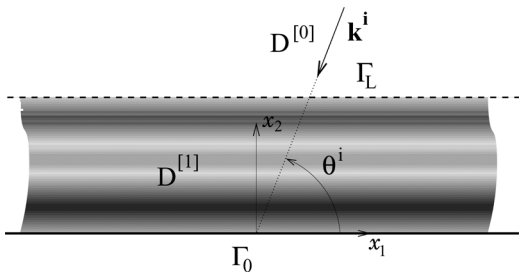

FIG. 1. Cross-sectional view of the configuration.

solution to the forward-scattering problem is ensured by the radiation condition

$$p^{[0]}(\mathbf{x}) - p^{i}(\mathbf{x}) \sim \text{outgoing waves}; |\mathbf{x}| \to \infty, x_2 > L. \tag{4}$$

B. The state vector formalism and Peano series expansion

The spatial Fourier transform $\hat{s}(x_2, k_1)$ of $s(\mathbf{x})$ is first introduced. This transform can be written in the form $s(\mathbf{x}) = \hat{s}(x_2, k_1)e^{ik_1x_1}$ for a plane wave. Henceforth, we drop the k_1 in $\hat{s}(x_2, k_1)$ so that it is written $\hat{s}(x_2)$.

Contrary to problems requiring the solution of the full macroscopic inhomogeneous poroelastic equations,[7] for which the choice of the state vector is conditioned by the boundary problem, those only requiring the solution of the equations under the rigid frame approximation can be naturally written in terms of the spatial Fourier transform of both the pressure and the normal component of the equivalent velocity. Effectively, the normal component of the equivalent velocity vector, $V_2^{[1]}$, and the pressure, $p^{[1]}$, are continuous along the x_2-axis inside the domain $D^{[1]}$, the normal component of the equivalent velocity vector and the pressure are continuous across Γ_L, and the normal component of the equivalent velocity vector vanishes on Γ_0. It seems natural to choose the spatial Fourier transform of these two parameters as components of the state vector. The procedure is briefly described below.

The spatial Fourier transform of Eq. (1) is

$$\begin{cases} \mathrm{i}\omega\hat{p}^{[1]} = \tilde{K}_{eq}(x_2)\left(\mathrm{i}k_1\hat{V}_1^{[1]} + \dfrac{\partial\hat{V}_2^{[1]}}{\partial x_2}\right), \\ \mathrm{i}\omega\tilde{\rho}_{eq}(x_2)\hat{V}_1^{[1]} = \mathrm{i}k_1\hat{p}^{[1]}, \\ \mathrm{i}\omega\tilde{\rho}_{eq}(x_2)\hat{V}_2^{[1]} = \dfrac{\partial\hat{p}^{[1]}}{\partial x_2}. \end{cases} \tag{5}$$

From the second equation of system (5), $\hat{V}_1^{[1]}$ can be expressed in terms of $\hat{p}^{[1]}$ through $\hat{V}_1^{[1]} = k_1\hat{p}^{[1]}/\omega\tilde{\rho}_{eq}(x_2)$. This expression can be substituted in the first equation of this system. The problem also reduces to the solution of the first order differential matrix system for the column state vector $\widehat{\mathbf{W}} = \langle\hat{p}^{[1]}, \hat{V}_2^{[1]}\rangle$, which takes the form

$$\frac{\partial}{\partial x_2}\widehat{\mathbf{W}} - \begin{bmatrix} 0 & \mathrm{i}\omega\tilde{\rho}_{eq}(x_2) \\ \dfrac{\mathrm{i}\omega}{\tilde{K}_{eq}(x_2)}\left(1 - \left(\dfrac{k_1}{\tilde{k}_{eq}(x_2)}\right)^2\right) & 0 \end{bmatrix} \cdot \widehat{\mathbf{W}} = \frac{\partial}{\partial x_2}\widehat{\mathbf{W}} - \mathbf{A}\cdot\widehat{\mathbf{W}} = 0, \tag{6}$$

where $\tilde{k}_{eq}(x_2) = k^{[1]} = \omega\sqrt{\tilde{\rho}_{eq}(x_2)/\tilde{K}_{eq}(x_2)}$. The matrix $\mathbf{A}$ is x_2-dependent, because $\Omega(x_2)$, $q^2(x_2)$, $R_b(x_2)$, and $\sigma(x_2)$, are x_2-dependent. Once the system (6) is solved, $V_1^{[1]}$ can then be evaluated.

The solution of system (6) takes the following matrix form:

$$\widehat{\mathbf{W}}(L) = \mathbf{M}\cdot\widehat{\mathbf{W}}(0), \tag{7}$$

where $\mathbf{M}$ is the so-called matricant,[14] which relates the value of the state vector $\widehat{\mathbf{W}}(0)$, at $x_2 = 0$, to the value of the state vector $\widehat{\mathbf{W}}(L)$, at $x_2 = L$. Since $\mathbf{A}$ is x_2 dependent (i.e., the plate is not homogeneous or piecewise constant) and $\mathbf{A}$ does not commute for different values of x_2, i.e., $[\mathbf{A}(x_2), \mathbf{A}(x_2')] = \mathbf{A}(x_2)\mathbf{A}(x_2') - \mathbf{A}(x_2')\mathbf{A}(x_2) \neq 0$, $\forall(x_2, x_2') \in [0, L]^2$, $x_2 \neq x_2'$, the matricant $\mathbf{M}$ does not contain matrix exponentials or multiplications of matrix exponentials. The matricant is rather defined by the so-called multiplicative integral satisfying the Peano expansion.[10,14–16] This avoids any problem related to lack of discretization when the continuously varying material is approximated by a piecewise constant material. The Peano series reads as

$$\mathbf{M} = \mathbf{I} + \int_0^L \mathbf{A}(x_2)\mathrm{d}x_2 + \int_0^L \mathbf{A}(x_2)\left(\int_0^{x_2}\mathbf{A}(\zeta)\mathrm{d}\zeta\right)\mathrm{d}x_2 + \cdots \tag{8}$$

and its evaluation is performed via the following iterative scheme:

$$\begin{cases} \mathbf{M}^{\{0\}} = \mathbf{I}, \\ \mathbf{M}^{\{n\}} = \mathbf{I} + \displaystyle\int_0^L \mathbf{A}(x_2)\mathbf{M}^{\{n-1\}}(x_2)\mathrm{d}x_2, \end{cases} \tag{9}$$

such that $\lim_{n\to\infty}\mathbf{M}^{\{n\}} = \mathbf{M}$.

C. The boundary value problem

The application of the boundary conditions at both interfaces Γ_L [continuity of pressure $\hat{p}^{[1]}(L) = \hat{p}^{[0]}(L)$ and normal component of the velocity $\hat{V}_2^{[1]}(L) = (1/1\rho^{[0]})(\partial\hat{p}^{[0]}(x_2)/\partial x_2)|_{x_2=L}$] and $\Gamma_0(\hat{V}_2^{[1]}(0) = 0)$ yields the state vectors $\widehat{\mathbf{W}}(L)$ and $\widehat{\mathbf{W}}(0)$, which are required to solve the problem. Separating the variables and making use of the radiation conditions it is possible to express the spatial Fourier transform of the pressure field in $D^{[0]}$ in the following form:

$$\hat{p}^{[0]} = e^{-\mathrm{i}k_2^{[0]}(x_2-L)} + Re^{\mathrm{i}k_2^{[0]}(x_2-L)}, \tag{10}$$

where R is the acoustic plane wave reflection coefficient. The state vectors become

$$\widehat{\mathbf{W}}(L) = \mathbf{S} + \mathbf{L}^L R \quad \text{and} \quad \widehat{\mathbf{W}}(0) = \mathbf{L}^0\cdot\hat{p}^{[1]}(0), \tag{11}$$

wherein $\mathbf{S}$ accounts for the excitation of the system by the plane incident wave, $\mathbf{L}^L$ relates the unknown R to the state vector $\widehat{\mathbf{W}}(L)$, and $\mathbf{L}^0$ relates the unknown $\hat{p}^{[1]}(0)$ to the state vector $\widehat{\mathbf{W}}(0)$. Their expressions are

$$\mathbf{S} = \begin{bmatrix} 1 \\ -k_2^{[0]}/\omega\rho^{[0]} \end{bmatrix}, \quad \mathbf{L}^0 = \begin{bmatrix} 1 \\ 0 \end{bmatrix}, \quad \text{and} \quad \mathbf{L}^L = \begin{bmatrix} 1 \\ \dfrac{k_2^{[0]}}{\omega\rho^{[0]}} \end{bmatrix}. \tag{12}$$

Finally, the introduction of Eq. (11) in Eq. (7) gives rise to the final system of equations, whose solution contains the reflection coefficient R

$$[[\mathbf{L}^L][-\mathbf{M}\cdot\mathbf{L}^0]]\cdot\begin{bmatrix} R \\ \hat{p}^{[1]}(0)\end{bmatrix} = -\mathbf{S}. \tag{13}$$

This system is solved for each frequency and directly provides the reflection coefficient associated with the plane incident wave. The pressure field in $D^{[0]}$ can then be calculated through $p^{[0]} = \hat{p}^{[0]}e^{ik_1x_1}$. A similar approach can be followed when the inhomogeneous porous plate is not backed and the sound waves can propagate into the air. In this case, a transmitted field is required and the transmission coefficient is also calculated.

This numerical procedure is robust. It has been validated by comparing the results obtained by the present method to those calculated by the classical transfer matrix method[2] at both normal and oblique incidence for a known two-layer porous material, modeled with the usual Johnson–Champoux–Allard model,[11,12] considered as a single inhomogeneous layer. It has also been validated by comparing the results obtained by the present method against those calculated by the wave splitting method together with the invariant embedding and compact Green's function as described in De Ryck *et al.*[4] In this analysis the method was tested on the material with continuously varying parameters describing the behavior of log-normal pore size distribution for which the acoustical model was proposed by Horoshenkov and Swift.[6]

IV. EXPERIMENTAL PROCEDURE

A. Sample preparation

The material sample investigated in this work was manufactured in the Acoustics Laboratory at the University of Bradford. A composition of a polyurethane binder (Chemique Adhesive, XP 2261green), polyol and tire shred residue (supplied by Credential Tyre Recycling, Ltd.) was used to produce this material. The material kinetics and experimental method are explained in the work by Masaharanon *et al.*[3] However, in this formulation polyol was an ether-based polyol with a lower molecular weight of 400. On the contrary, polyol with a molecular weight of 600 was investigated in the work by Masaharanon *et al.*[3] When a low molecular weight polyol is used, then the reaction is faster, leading to a more rigid structure which traps more of the CO_2 gas into smaller pores. Higher molecular weight polyols, on the other hand, will react more slowly, creating a softer and more flexible structure which allows the formation of more comparatively larger, open pores.

The chemical formulation described in the above paragraph was poured in a round mold which was closed at one end and open at the other end. The diameter of this mold was 100 mm and its height 150 mm. When the chemical reaction was finished, the resultant porous sample was removed from the mold and its top and bottom surfaces were trimmed with a sharp knife to form a 140 mm long porous cylinder with smooth top and bottom surfaces. Photographs of the resultant material sample (porous cylinder) and its top and bottom surfaces are shown in Fig. 2.

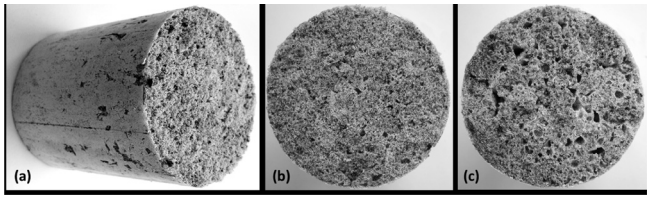

FIG. 2. Photographs of the 140 mm thick material sample with pore stratification: (a) original 140 mm porous cylinder; (b) top surface of the sample consisting of smaller pores; (c) bottom surface of the sample consisting of larger pores.

B. Material characterization procedure

The acoustical and related non-acoustical properties of the material sample were determined using the following procedure. First, the acoustical absorption coefficient of the original 140 mm porous cylinder was measured in the direct and reverse orientations. This experiment was carried out in a 100 mm diameter, two-microphone Bruel & Kjael (BK4206) impedance tube at normal angle of incidence and in the frequency range of 100−1600 Hz using the standard procedure detailed in Ref. 17. The reproducibility of this experiment is within $\pm 1-2\%$. The direct orientation corresponded to the case when the acoustic excitation in the impedance tube was applied to the top surface of the sample which contained smaller pores. The reverse orientation was the opposite, i.e., when the acoustic excitation was applied to the bottom surface of the material sample, i.e., to the surface that consisted of larger pores. Secondly, the porous cylinder was sliced into four sub-layers each having the thickness of 35 mm. The acoustical properties of each of these four sub-layers were measured in the impedance tube in the direct and reverse orientations to study the effect of pore stratification. Figure 3 shows microscopic photographs of the top and bottom surfaces of the four sub-layers which were obtained by slicing the original 140 mm material specimen into four individual parts. These adjacent images clearly illustrate the pore stratification which was achieved with this material manufacturing process. Here, the larger pores occur

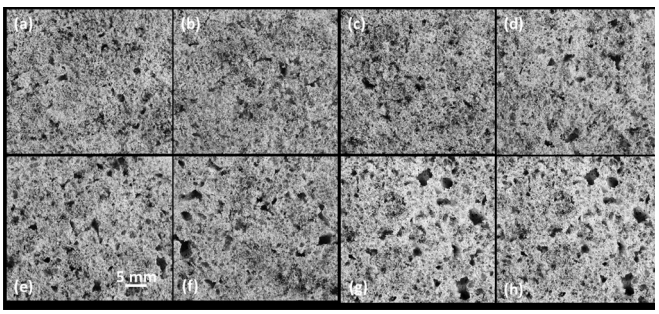

FIG. 3. Microscopic photographs of the porous surfaces of the four sub-layers in which the 140 mm sample was divided. The order of the images is from the upper surface of the top sublayer (a), successively to the lower surface of the bottom sublayer (h). Photographs (b) and (c); (d) and (e); (f) and (g) correspond to adjacent internal surfaces.

in the bottom layer whereas the pores in the top layer are evidently smaller.

The measured acoustic absorption coefficient data for each individual sub-layer were input in a standard optimization algorithm to deduce the flow resistivity, R_b, porosity, Ω, tortuosity, q^2, and standard deviation in the pore size, σ. An objective function was adopted to minimize the following difference:

$$F(\mathbf{z}) = \sum_{n=1}^{N} |\alpha_{exp}(f_n) - \alpha_{th}(f_n, \mathbf{z})| \rightarrow \min, \tag{14}$$

where f_n are the frequencies in the experimentally determined acoustic absorption coefficient spectrum and $\alpha_{exp}(f_n)$, $\mathbf{z} = \{R_b, \Omega, q, \sigma\}$ is the design variable vector. The optimization algorithm was based on the Nelder–Mead direct search optimization method detailed in Ref. 18. This parameter inversion was carried out for $N = 750$ in the frequency range of 100–1600 Hz that is a standard operational range for an impedance tube with a 100 mm diameter. The non-acoustical parameters deduced from the optimization analysis for the four porous sub-layers are presented in Table I. Figure 4 presents a comparison between the measured absorption coefficient spectra for the four sub-layers and absorption coefficient spectra predicted using the values of non-acoustical parameters listed in Table I. Here, the depth measurement corresponds to the direction x_2 which increases towards the top of the material specimen. The index shown in brackets in column 1 in Table I represents the sub-layer number.

The following conclusions can be drawn from these results (Table I and Fig. 4) and from the analysis of the images shown in Fig. 3. First, there is a good agreement between the measured and predicted absorption coefficient for each of the four individual sub-layers. There is a relatively small stratification within a single sub-layer so that the model captures well its acoustical behavior observed in the direct and in reverse orientations. Secondly, the material porosity is relatively independent of the depth. Thirdly, the flow resistivity increases considerably with the increased layer depth and the flow resistivity of the top sub-layer is approximately five times higher than at the top. Fourthly, there is a rather complex dependence of the tortuosity and standard deviation in the pore size on the layer depth. The

TABLE I. The values of the four non-acoustical parameters as a function of the layer depth.

Layer depth, x_2 (mm)	Micrograph, Fig. 3	Ω	q^2	R_b (N s m^{-4})	σ
140 (1)	(a)	0.757	2.236	125 200	0.570
105 (1)	(b)	0.731	2.800	117 600	0.633
105 (2)	(c)	0.702	1.725	64 000	1.199
70 (2)	(d)	0.718	1.017	46 730	1.613
70 (3)	(e)	0.738	2.245	57 730	0.807
35 (3)	(f)	0.740	1.606	43 780	1.183
35 (4)	(g)	0.768	1.976	29 110	0.635
0 (4)	(h)	0.745	1.803	24 520	0.761

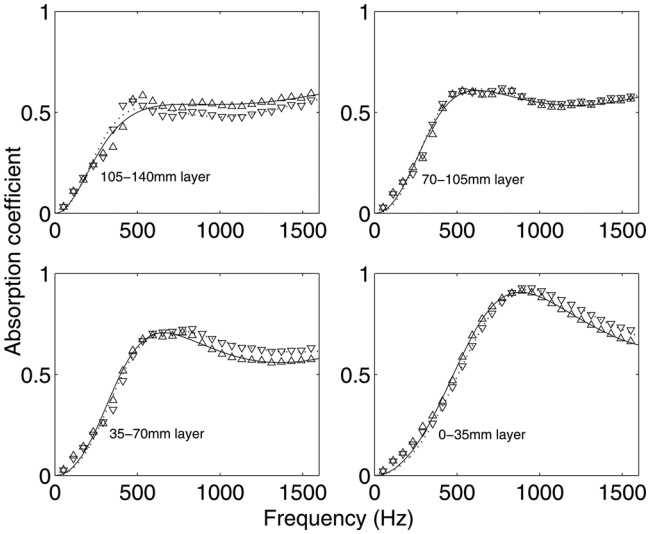

FIG. 4. The measured and predicted acoustic absorption coefficient spectra for direct and reverse orientations of the four porous sub-layers [△: measured data (direct orientation); ▽: measured data (reverse orientation); —: predicted (direct orientation); …: predicted (reverse orientation)].

structure of the material appears less tortuous near the middle and more tortuous near the ends. This can be explained by a larger proportion of partly closed pores near the open ends and by a more complex interconnectivity between pores of different pore sizes observed in this part of the material specimen in the optical images. An opposite type of the behavior is observed in the standard deviation in the pore size distribution data, which peaks at the medium depth where the minimum tortuosity value is also observed (see Table I). This phenomenon is difficult to interpret without accurate pore size distribution data and it deserves a more detailed investigation.

V. NUMERICAL RESULTS

In order to facilitate the calculations each parameter in Fig. 6 was discretized in 1000 points and the number of iterations for the evaluation of the Peano series was fixed at 250. These values were not optimized, but it was found that the spatial discretization along the inhomogeneity should be small compared to the wavelength inside the porous material for the method to model the response correctly. This method is computationally efficient in case of rigid frame approximation problems.

Each parameter P is approximated by a fourth order polynomial function of $P(x_2) = a_P x_2^4 + b_P x_2^3 + c_P x_2^2 + d_P x_2 + e_P$ (Lagrangian), whose coefficients, a_P, b_P, c_P, d_P, and e_P have been obtained by matching the polynomial function with a parameter value measured at a specific depth. The parameters at both edges of the sample are fixed at their values at the depths of 140 and 0 mm. At each of the three cutting depths (105, 70, and 35 mm), two parameters values are available: one corresponds to the upper sub-layer in the reversed orientation and the other to the lower sub-layer in the direct orientation (see Table I). The generated profile with the fourth order polynomial function is sensitive to the choice of these values. Figure 5 depicts the profiles generated when the value at cutting

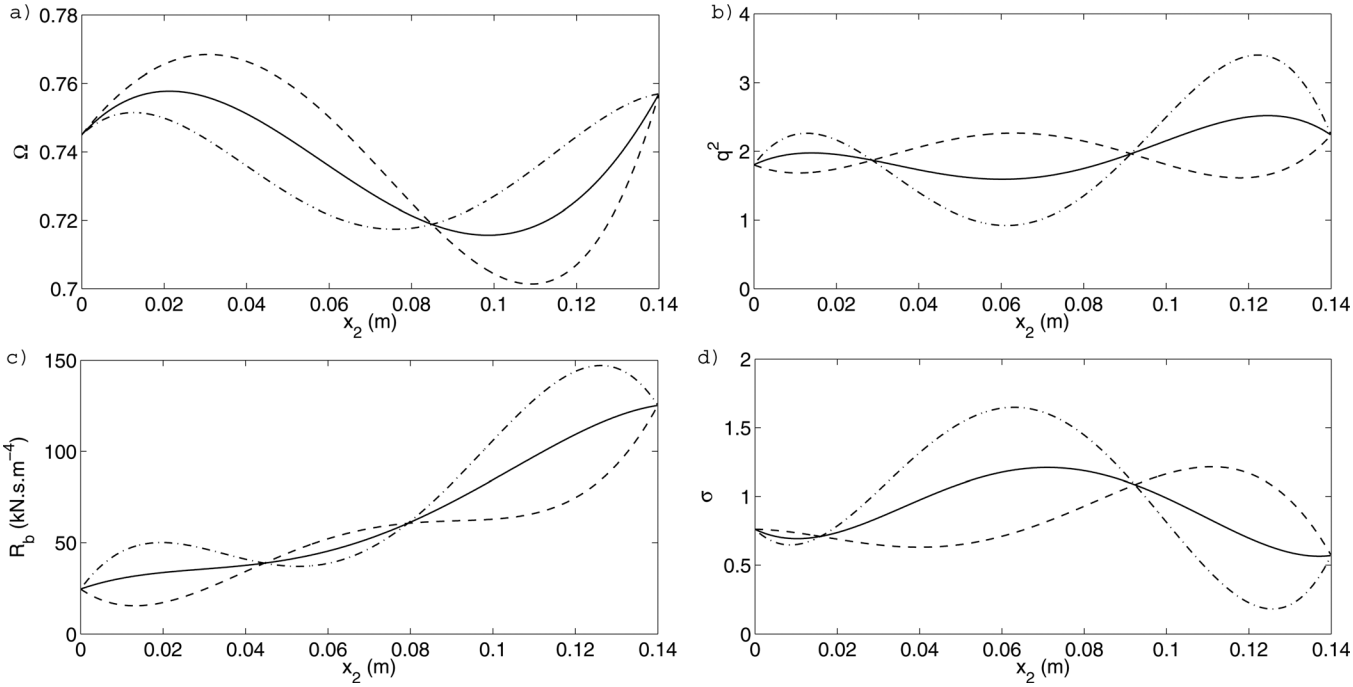

FIG. 5. Polynomial fits of (a) the porosity Ω, (b) the tortuosity q^2, (c) the flow resistivity R_b, and (d) the standard deviation in the pore size σ, as a function of sample depth. Experimental points were at the surface positions of each sub-layer, derived from (—) the mean values measured for the upper sub-layer in the reversed orientation and of the lower sub-layer in the direct orientation, (– – –) the value of the lower sub-layer in the direct orientation and (– · –) the value of the upper sub-layer in the reversed orientation (see Table I).

depth is (i) the mean values of the upper sub-layer in the reversed orientation and of the lower sub-layer in the direct orientation; (ii) the value of the lower sub-layer in the direct orientation; and (iii) the value of the upper sub-layer in the reversed orientation.

Figure 6 depicts the absorption coefficient (A) calculated with the proposed theoretical model [$A = 1 - R^2$, R is the solution of Eq. (13)] for the parameter profiles shown in Fig. 5 and the measured absorption coefficients for the whole material sample. Several observations can be made on the basis of these results. First, the model captures well the behavior of the measured acoustic absorption coefficient spectra throughout the considered frequency range. Secondly, the agreement between the model and the measured data is better in the case of direct sample orientation, i.e., when the sound wave is incident on the higher flow resistivity end of the sample. Thirdly, a better agreement between the modeled and measured data is obtained when the parameter values for the upper sliced sample in the reverse orientation are used (see dash-dotted lines in Fig. 5). Fourthly, the largest discrepancy between the modeled and measured data is observed when the parameter values for the lower sliced sample in the direct orientation are used in the model. Fifthly, the mean parameter values enable the model to provide a sufficiently close fit (within 5%). The observed discrepancies are generally small and can be explained by the choice of the method to generate the parameter profiles shown in Fig. 5. A modification of one value in the parameter profile leads to the modification of the profile as a whole and different coefficients in the Lagrangian which need to be

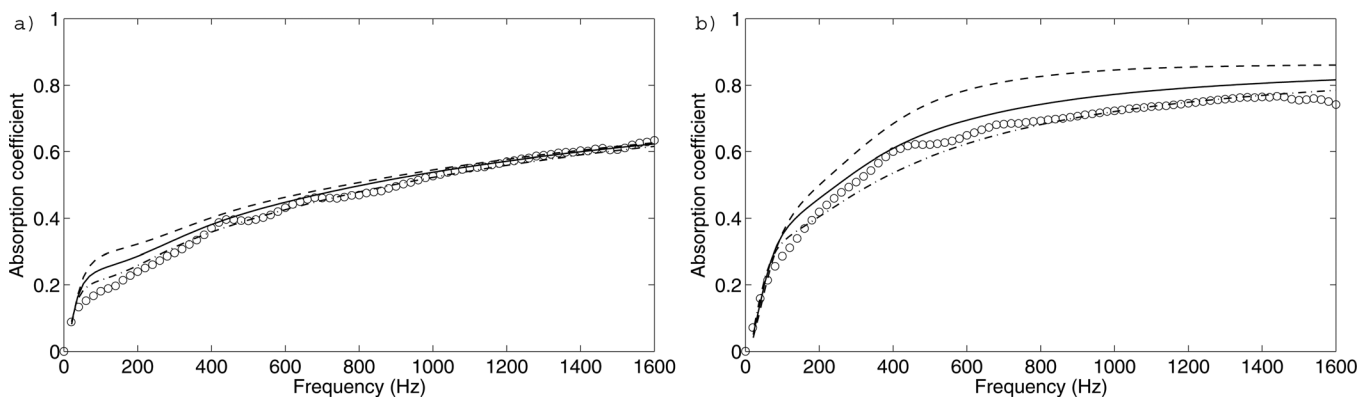

FIG. 6. Normal incidence absorption coefficient of the 140 mm thick sample in (a) the direct and (b) the reverse orientations. (○) measured. (—) calculated when the value at each cutting depth is the mean values of the upper sliced sample in the reversed orientation and of the lower sliced sample in the direct orientation, (– – –) calculated when the value of the lower sliced sample in the direct orientation, and (– · –) calculated when the value of the upper sliced sample in the reversed orientation.

adopted in the polynomial approximation. The values of these parameters depend to some extent on the sub-layer orientation. Clearly, there is small inhomogeneity within each of the four sub-layers and it may be necessary to refine further the material characterization procedure which was used to determine the stratification parameters shown in Table I.

The absorption coefficient data measured for the direct and reverse sample orientations (see Fig. 5) are markedly different. This indicates that the sample is macroscopically inhomogeneous. The absorption coefficient spectrum measured in the reverse sample orientation (A_r) is consistently higher than that measured in the direct orientation (A_d). It is possible to illustrate with these data that the ratio of these two absorption coefficient spectra has a clear peak $\max\{A_r/A_d\} \approx 1.8$ which occurs around 220 Hz. Beyond this peak the ratio of the two spectra asymptotically approaches $A_r/A_d \rightarrow 1.2$ at 1600 Hz. This phenomenon can be mainly explained by the change in the air flow resistivity, which increases gradually from $x_2 = 0$ mm to $x_2 = 140$ mm and this increase is approximately five-fold. When the incident wave strikes at the sample in the direct orientation, the value of R_b is relatively large resulting in a poor impedance mismatch ($R_b L/\rho_0 c \approx 41$). In this case a considerable amount of the acoustic energy in the incident wave is reflected at the interface $x_2 = L$ and the spectrum of the absorption coefficient is limited. In the case, when the wave strikes in the reverse orientation (at $x_2 = 0$), the value of R_b is relatively small and it gradually increases with depth. There is a smaller impedance mismatch ($R_b L/\rho_0 c \approx 8$). Therefore, the strength of the reflection is smaller and the absorption coefficient is relatively large. While R_b changes considerably with depth, the stratification in the other three non-acoustical parameters, as a first approximation, is relatively small. Numerical simulations suggest that there is little difference between the absorption coefficient spectra predicted with the actual profiles for $\Omega(x_2)$, $q(x_2)$, and $\sigma(x_2)$ as shown in Fig. 5, and those predicted with their depth-averaged values. Clearly, the effect of $R_b(x_2)$ on the observed acoustic absorption coefficient spectra is dominant here. This parameter is controlled directly by the pore size distribution which changes as a function of depth. This effect seems to be well predicted by the pore size distribution model and alternative Biot's formulation approach adopted in Sec. II.

VI. CONCLUSIONS

This work presents new experimental data on the acoustic absorption coefficient of a material with continuous pore stratification. This material has been manufactured using a relatively simple chemical reaction process in which a mixture of recycled grains and fibers has been bonded with a polyurethane binder. The acoustical properties and related non-acoustical parameters of the resultant porous structure have been measured and/or deduced. It has been shown that the acoustical properties of this sample presented in the direct and reverse orientations are markedly different so that the developed porous structure is macroscopically inhomogeneous. The absorption coefficient spectrum measured in the reverse sample orientation is up to 80% higher than that measured in the direct orientation. This variation in the absorption coefficient spectrum is associated with the variation in the impedance mismatch when the sample orientation is reversed.

The variations in the values of the measured non-acoustical parameters have been used to explain the observed acoustic absorption coefficient spectra and their dependence on the sample orientation. It has been shown that the effect of the flow resistivity on the observed acoustic absorption coefficient spectra is dominant. This parameter undergoes an approximately five-fold change through the 140 mm sample depth. A suitable theoretical model has been adopted to explain this effect. The adopted model is based on the alternative Biot's formulation[5] and pore size distribution model proposed by Horoshenkov and Swift.[6] This model makes use of the four non-acoustical parameters: flow resistivity, porosity, tortuosity, and standard deviation in the pore size which can vary as a function of sample depth. The model captures well the behavior of the measured acoustic absorption coefficient spectra throughout the considered frequency range with the accuracy of 5% or better. It has been shown that it is possible to use the parameter values which are averaged within a depth interval in which their variation is relatively small.

This work paves the way to the application of the method proposed by De Ryck *et al.*[19] to the inversion of the depth profiles of all non-acoustical parameters of this type of porous media. In this way the material characterization procedure which has been used in this work needs can be refined. At present, it is unclear how this refinement can be practically achieved. The reduction of the sub-layer thickness is unlikely to work because of the apparent increase in the measurement error associated with testing of a thin material specimen. There are a number of conflicting requirements here to be balanced: (i) the residual level of stratification within each of the four sub-layers should be relatively small; (ii) the thickness of each of the four sub-layers should be much greater than the maximum pore size in the material; (iii) the thickness of each of the four sub-layers should be large enough to enable accurate measurements of the acoustical and non-acoustical properties using the standard material characterization methods. It is believed that the pragmatic material characterization approach adopted in this work provides a reasonable balance to the requirements highlighted above.

ACKNOWLEDGMENTS

The authors are grateful to Professor David C. Hothersall for his useful comments on this manuscript. This work was partly supported by EU FP7 HOSANNA (Project No. 234306).

[1]U. Ingard, *Sound Absorption Technology* (Noise Control Foundation, New York, 1994), Chap. 3.2.
[2]B. Brouard, D. Lafarge, and J.-F. Allard, "A general method of modelling sound propagation in layered media," J. Sound Vib. **183**, 129–142 (1995).

[3]S. Mahasaranon, K. V. Horoshenkov, A. Khan, and H. Benkreira, "The effect of continuous pore stratification on the acoustic absorption in open cell foams," J. Appl. Phys. **111**, 084901 (2012).
[4]L. De Ryck, W. Lauriks, Z. Fellah, A. Wirgin, J. Groby, P. Leclaire, and C. Depollier, "Acoustic wave propagation and internal fields in rigid frame macroscopically inhomogeneous porous media," J. Appl. Phys. **102**, 024910 (2007).
[5]M. Biot, "Mechanics of deformation and acoustic propagation in porous media," J. Appl. Phys. **33**, 1482–1498 (1962).
[6]K. Horoshenkov and M. Swift, "The acoustic properties of granular materials with pore size distribution close to log-normal," J. Acoust. Soc. Am. **110**(5), 2371–2378 (2001).
[7]G. Gautier, J. Groby, O. Dazel, L. Kelders, L. Deryck, and P. Leclaire, "Propagation of acoustic waves in a one-dimensional macroscopically inhomogeneous poroelastic material," J. Acoust. Soc. Am. **130**, 1390–1398 (2011).
[8]A. Shuvalov, O. Poncelet, and M. Deschamps, "General formalism for plane guided waves in transversely inhomogeneous anisotropic plates," Wave Motion **40**, 413–426 (2004).
[9]A. Shuvalov, O. Poncelet, M. Deschamps, and C. Baron, "Long-wavelength dispersion of acoustic waves in transversely inhomogeneous anisotropic plates," Wave Motion **42**, 367–382 (2005).
[10]A. Shuvalov, E. Le Clezio, and G. Feuillard, "The state-vector formalism and the Peano-series solution for modelling guided waves in functionally graded anisotropic piezoelectric plates," Int. J. Eng. Sci. **46**, 929–947 (2008).
[11]J.-F. Allard and Y. Champoux, "New empirical equations for sound propagation in rigid frame porous materials," J. Acoust. Soc. Am. **91**, 3346–3353 (1992).
[12]D. Johnson, J. Koplik, and R. Dashen, "Theory of dynamic permeability and tortuosity in fluid-saturated porous media," J. Fluid Mech. **176**, 379–402 (1987).
[13]G. Pispola, K. H. Horoshenkov, and A. Khan, "Comparison of two modeling approaches for highly heterogeneous porous media," J. Acoust. Soc. Am. **121**, 961–966 (2007).
[14]M. Pease, *Methods of Matrix Algebra* (Academic Press, New York, 1965), Chaps. 6 and 7.
[15]C. Baron, "Matricant Peano series development to study elastic waves propagation in continuously varying properties materials," Ph.D. thesis, Université de Bordeaux I, 2005 (in French).
[16]G. Peano, "Integration of linear differential equations by series expansion (in French)," Math. Ann. **32**, 450–456 (1888).
[17]ISO 10534: *Acoustics: Determination of Sound Absorption Coefficient and Impedance in Impedance Tubes—Part 2: Transfer Function Method* (International Organization for Standardization, Geneva, 2001).
[18]J. A. Nelder and R. Mead, "A simplex method for function minimization," Comput. J. **7**, 308–313 (1965).
[19]L. De Ryck, W. Lauriks, P. Leclaire, J. P. Groby, A. Wirgin, and C. Depollier, "Reconstruction of material properties profiles in one-dimensional macroscopically inhomogeneous rigid frame porous media in the frequency domain," J. Acoust. Soc. Am. **124**, 1591–1606 (2008).